






Generation of a μ -1,2-hydroperoxo $\text{Fe}^{\text{III}}\text{Fe}^{\text{III}}$ and a μ -1,2-peroxo $\text{Fe}^{\text{IV}}\text{Fe}^{\text{III}}$ Complex

Stephan Walleck¹, Thomas Philipp Zimmermann¹, Henning Hachmeister², Christian Pilger ², Thomas Huser ², Sagie Katz³, Peter Hildebrandt ³, Anja Stammeler¹, Hartmut Bögge¹, Eckhard Bill ⁴ & Thorsten Glaser ¹✉

μ -1,2-Peroxo-diferric intermediates (**P**) of non-heme diiron enzymes are proposed to convert upon protonation either to high-valent active species or to activated **P'** intermediates via hydroperoxo-diferric intermediates. Protonation of synthetic μ -1,2-peroxo model complexes occurred at the μ -oxo and not at the μ -1,2-peroxo bridge. Here we report a stable μ -1,2-peroxo complex $\{\text{Fe}^{\text{III}}(\mu\text{-O})(\mu\text{-1,2-O}_2)\text{Fe}^{\text{III}}\}$ using a dinucleating ligand and study its reactivity. The reversible oxidation and protonation of the μ -1,2-peroxo-diferric complex provide μ -1,2-peroxo $\text{Fe}^{\text{IV}}\text{Fe}^{\text{III}}$ and μ -1,2-hydroperoxo-diferric species, respectively. Neither the oxidation nor the protonation induces a strong electrophilic reactivity. Hence, the observed intramolecular C-H hydroxylation of preorganized methyl groups of the parent μ -1,2-peroxo-diferric complex should occur via conversion to a more electrophilic high-valent species. The thorough characterization of these species provides structure-spectroscopy correlations allowing insights into the formation and reactivities of hydroperoxo intermediates in diiron enzymes and their conversion to activated **P'** or high-valent intermediates.

¹Lehrstuhl für Anorganische Chemie I, Fakultät für Chemie, Universität Bielefeld, Universitätsstr. 25, D-33615 Bielefeld, Germany. ²Biomolekulare Photonik, Fakultät für Physik, Universität Bielefeld, Universitätsstr. 25, D-33615 Bielefeld, Germany. ³Institut für Chemie, Technische Universität Berlin, Straße des 17. Juni 135, D-10623 Berlin, Germany. ⁴Max-Planck-Institut für Chemische Energiekonversion, Stiftstr. 34-36, D-45470 Mülheim an der Ruhr, Germany. ✉email: thorsten.glaser@uni-bielefeld.de

Non-heme diiron enzymes are employed by nature to activate dioxygen for various catalytic oxidation and/or oxygenation reactions^{1,2}. Their catalytic cycles generally employ a diferrous form that reacts with dioxygen to a peroxo-diferric intermediate (**P**, Fig. 1a). The active species is supposed to be either this peroxo-diferric species or a species derived from it. In soluble methane monooxygenase (sMMO)^{3–5}, the peroxo intermediate **P** converts to a high-valent Fe^{IV}Fe^{IV} active species (**Q**, Fig. 1a)^{1–8}. Kinetic studies revealed a pH-dependence indicating that this step is proton-promoted^{1,3,9,10}. The site of protonation is still unknown. Proposals include protonation of the peroxo ligands resulting in bridging μ -1,1- or μ -1,2-hydroperoxo ligands^{2,3,9–11}. In other non-heme diiron enzymes^{12–20}, a peroxo activation step has been proposed by the conversion of **P**-type to **P'**-type intermediates that lack the peroxo \rightarrow Fe^{III} LMCT around 14,000–15,000 cm⁻¹ and the higher Mössbauer isomer shift characteristic for **P**-type intermediates. For this peroxo activation step, also a protonation has been suggested^{15,16,20}. For the two diiron arylamine oxygenases AurF and CmlI, μ -1,2-hydroperoxo¹⁵ and μ -1,1-peroxo intermediates²¹ have been proposed, respectively, or a μ -1,1-hydroperoxo intermediate for both (Fig. 1a)¹⁴.

Syntheses and detailed spectroscopy and reactivity studies of μ -1,2-peroxo-diferric model complexes^{22–35} provided not only important structure-spectroscopy correlations to establish peroxo intermediates in the enzymes but also variations in their stabilities and reactivities by slight variations of the ligands. In most cases, the μ -1,2-peroxo-diferric species could only be identified spectroscopically as transient intermediates. Interestingly, protonation of different complexes with a {Fe^{III}(μ -O)(μ -1,2-O₂)Fe^{III}} core afforded μ -hydroxo-bridged {Fe^{III}(μ -OH)(μ -1,2-O₂)Fe^{III}} species^{22,27,36} questioning the principle accessibility of hydroperoxo-diferric species.

Here, we present the synthesis, characterization, and reactivity of the rationally stabilized μ -1,2-peroxo complex [(susan^{6-Me})Fe^{III}(μ -O)(μ -1,2-O₂)Fe^{III}](ClO₄)₂ using the dinucleating ligand susan^{6-Me} (Fig. 1b)^{37–39}. This μ -1,2-peroxo complex is stable even in solution at -40 °C and shows nucleophilic character of the μ -1,2-peroxo ligand attenuated for exogenous organic substrates by encapsulation of the ligand scaffold. [(susan^{6-Me})Fe^{III}(μ -O)(μ -O₂)Fe^{III}]²⁺ is reversibly oxidized to the high-valent μ -1,2-peroxo complex [(susan^{6-Me})Fe^{IV}(μ -O)(μ -1,2-O₂)

Fe^{III}]³⁺ and reversibly protonated to the μ -1,2-hydroperoxo complex [(susan^{6-Me})Fe^{III}(μ -O)(μ -1,2-OOH)Fe^{III}]³⁺. The study of the electrophilic reactivity for oxygen-atom transfer (OAT) using PPh₃ and hydrogen-atom transfer (HAT) using DHA and TEMPOH provides not only a low electrophilic character of the parent μ -1,2-peroxo-Fe^{III}Fe^{III} complex but also for the oxidized μ -1,2-peroxo-Fe^{IV}Fe^{III} and protonated μ -1,2-hydroperoxo-Fe^{III}Fe^{III} species. Only the oxidized μ -1,2-peroxo-Fe^{IV}Fe^{III} species reacts with the relatively weak substrate TEMPOH. The determination of the $pK_a = 9.5 \pm 0.1$ and the bond dissociation free energy BDFE(OH)_{CH₃CN} = 78 \pm 2 kcal mol⁻¹ of the protonated μ -1,2-hydroperoxo-Fe^{III}Fe^{III} species quantifies the low electrophilic character even of the oxidized μ -1,2-peroxo-Fe^{IV}Fe^{III} species. Therefore, the intramolecular C–H activation of preorganized 6-methyl pyridine groups to benzylalcoholato and carboxylato donors in the parent 1,2-peroxo-Fe^{III}Fe^{III} complex should not occur via the 1,2-peroxo-ligand but via conversion to a more reactive but fluent high-valent species. The low electrophilic character and the spectroscopic signatures of this μ -1,2-hydroperoxo-diferric model are discussed in relation to assignments of reactive intermediates postulated for diiron enzymes.

Results

The complex [(susan^{6-Me})Fe^{III}(μ -O)(μ -1,2-O₂)Fe^{III}]²⁺. The reaction of susan^{6-Me} and Fe(ClO₄)₂·6H₂O provided [(susan^{6-Me})Fe^{II}(μ -OH)₂Fe^{II}](ClO₄)₂ (Fig. S1a) and subsequent reaction with O₂ at -15 °C the μ -1,2-peroxo complex [(susan^{6-Me})Fe^{III}(μ -O)(μ -1,2-O₂)Fe^{III}](ClO₄)₂ (Fig. 2a). Single-crystal X-ray diffraction provides an asymmetric core structure: the μ -1,2-peroxo ligand is coordinated with O1 trans to a tert-amine (N2) and with O2 trans to a pyridine (N44). This results in a shorter Fe1–O1^{peroxo} and a longer Fe2–O2^{peroxo} bond. The resulting different charge donation is compensated by a longer Fe1–O3^{oxo} and a shorter Fe2–O3^{oxo} bond. The O1–O2 bond length of 1.432(2) Å is the longest yet established for a peroxo-diferric complex (1.396–1.426 Å)^{22–26}.

Despite this structural asymmetry, the Mössbauer spectrum exhibits one quadrupole doublet with isomer shift $\delta = 0.53$ mm s⁻¹ and quadrupole splitting $|\Delta E_Q| = 1.69$ mm s⁻¹ (Fig. 2b and Fig. S7). This isomer shift is higher than 0.47 mm s⁻¹ of [(susan^{6-Me})Fe^{III}F(μ -O)Fe^{III}F]²⁺ (Table 1)⁴⁰, which is in line with higher values frequently observed for peroxo-diferric complexes^{1,41}. Magnetic measurements (Fig. 2c) revealed an exchange coupling of $J = -155$ cm⁻¹ (in the convention $H = -2J S_1 S_2$) providing an exact value for a μ -1,2-peroxo, μ -oxo-diferric complex. This antiferromagnetic coupling is significantly stronger than -100 ± 20 cm⁻¹ usually found for μ -oxo-diferric complexes^{42,43} including those with our dinucleating ligands³⁸. This applies also to μ -oxo, μ -carboxylato-diferric complexes which exhibit decreased $\angle(\text{Fe}^{\text{III}}-\mu\text{-O})-\text{Fe}^{\text{III}}$ angles as the μ -1,2-peroxo, μ -oxo-diferric complex. This comparison indicates a significant contribution of the Fe^{III}- μ -1,2-peroxo-Fe^{III} exchange pathway due to shorter (1.88 and 1.93 Å) and hence more covalent Fe^{III}- μ -O^{peroxo} bonds⁴⁴ compared to the longer Fe^{III}- μ -carboxylato bonds (e.g., 1.97 and 2.07 in [(susan){Fe^{III}(μ -O)(μ -OAc)Fe^{III}]³⁺)⁴⁵ that are considered not to contribute significantly to the exchange coupling.

The UV-Vis-NIR spectrum (Fig. 2d) exhibits three prominent bands at 19,300 cm⁻¹ ($\epsilon = 1180$ M⁻¹ cm⁻¹), 15,400 cm⁻¹ ($\epsilon = 1000$ M⁻¹ cm⁻¹), and 11,800 cm⁻¹ ($\epsilon = 190$ M⁻¹ cm⁻¹) that are characteristic for {Fe^{III}(μ -O)(μ -1,2-O₂)Fe^{III}} complexes²⁹ with the 19,300 cm⁻¹ band assigned to the μ -oxo \rightarrow Fe^{III} LMCT and the 15,400 cm⁻¹ band to the μ -1,2-peroxo \rightarrow Fe^{III} LMCT involving $\pi^*_{\pi} \rightarrow t_{2g}$ transitions¹¹. This low LMCT energy demonstrates strong covalency of the Fe^{III}-O^{peroxo} bond representing the origin of the strong antiferromagnetic coupling.

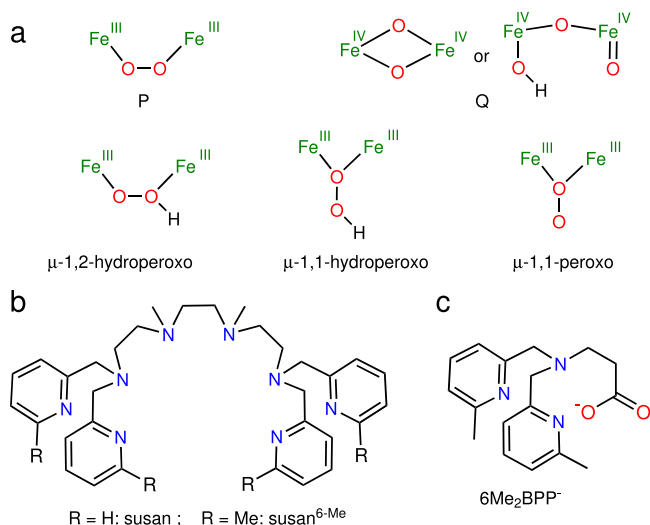


Fig. 1 Structural formula. **a** Supposed intermediates in non-heme diiron enzymes. **b** The dinucleating ligands susan and susan^{6-Me}. **c** The mononucleating ligand 6Me₂BPP⁻.

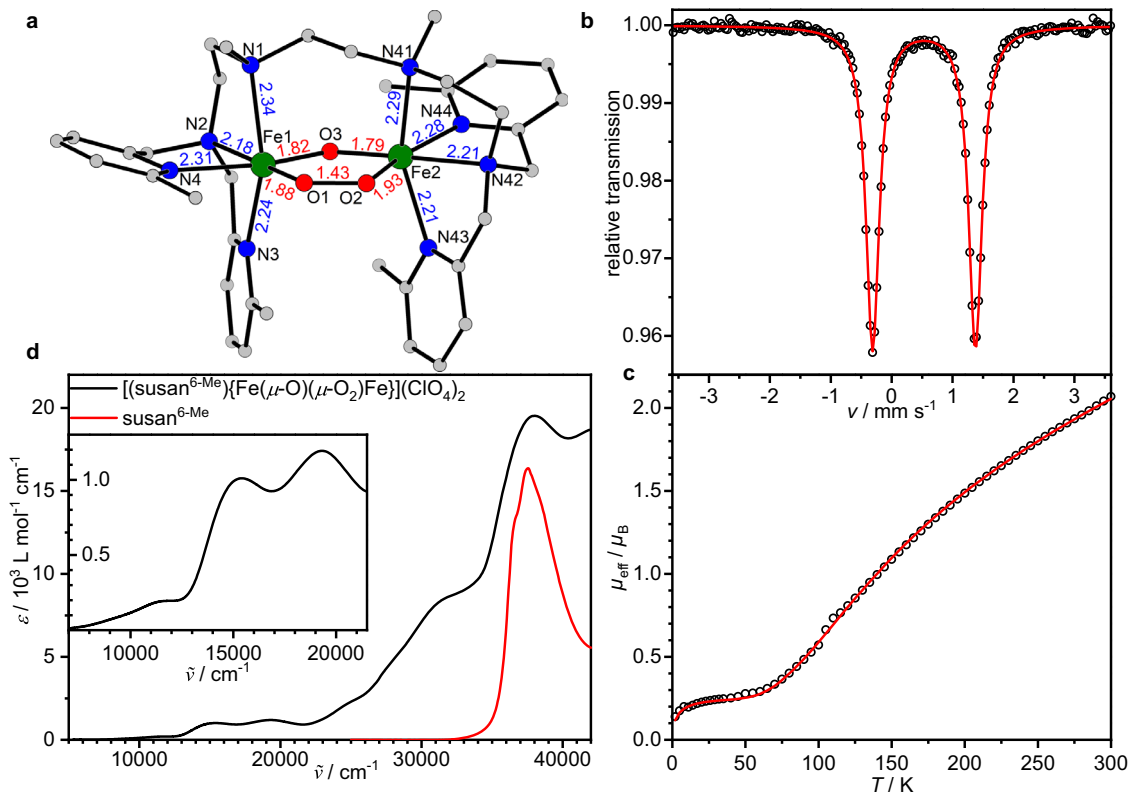


Fig. 2 Characterization of $[(\text{susan}^{6\text{-Me}})\{\text{Fe}^{\text{III}}(\mu\text{-O})(\mu\text{-O}_2)\text{Fe}^{\text{III}}\}](\text{ClO}_4)_2$. **a** Molecular structure of $[(\text{susan}^{6\text{-Me}})\{\text{Fe}^{\text{III}}(\mu\text{-O})(\mu\text{-O}_2)\text{Fe}^{\text{III}}\}]^{2+}$ in single-crystals of $[(\text{susan}^{6\text{-Me}})\{\text{Fe}^{\text{III}}(\mu\text{-O})(\mu\text{-O}_2)\text{Fe}^{\text{III}}\}](\text{ClO}_4)_2 \cdot 0.85\text{CH}_3\text{CN} \cdot 0.7\text{H}_2\text{O}$. Hydrogen atoms have been omitted for clarity. **b** ^{57}Fe Mössbauer spectrum of $[(\text{susan}^{6\text{-Me}})\{\text{Fe}^{\text{III}}(\mu\text{-O})(\mu\text{-O}_2)\text{Fe}^{\text{III}}\}](\text{ClO}_4)_2$ at 80 K. The solid line is a simulation with $\delta = 0.53 \text{ mm s}^{-1}$, $|\Delta E_Q| = 1.69 \text{ mm s}^{-1}$, and $\Gamma = 0.26 \text{ mm s}^{-1}$. **c** Temperature-dependence of the effective magnetic moment, μ_{eff} , of $[(\text{susan}^{6\text{-Me}})\{\text{Fe}^{\text{III}}(\mu\text{-O})(\mu\text{-O}_2)\text{Fe}^{\text{III}}\}](\text{ClO}_4)_2$. The solid line is a simulation to the spin-Hamiltonian (1) in the Supplementary Information with $J = -155 \text{ cm}^{-1}$, $g_1 = 2.05$, 0.2% p.i. ($S = 5/2$) of same molecular mass and $\theta_{w,\text{pi}} = -8 \text{ K}$. **d** UV-Vis-NIR spectrum of $[(\text{susan}^{6\text{-Me}})\{\text{Fe}^{\text{III}}(\mu\text{-O})(\mu\text{-O}_2)\text{Fe}^{\text{III}}\}](\text{ClO}_4)_2$ dissolved in CH_3CN at $-10 \text{ }^\circ\text{C}$ and the ligand $\text{susan}^{6\text{-Me}}$ for comparison.

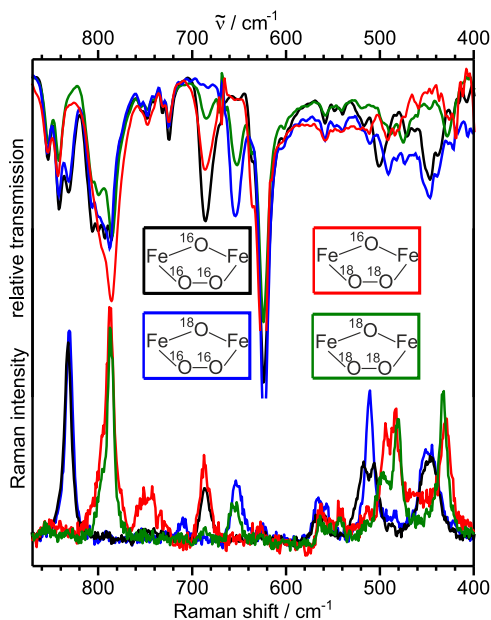


Fig. 3 Vibrational characterization of $[(\text{susan}^{6\text{-Me}})\{\text{Fe}^{\text{III}}(\mu\text{-O})(\mu\text{-O}_2)\text{Fe}^{\text{III}}\}](\text{ClO}_4)_2$. Resonance Raman (bottom, 633 nm ($15,800 \text{ cm}^{-1}$) excitation) and FTIR spectra (top) measured on solids at room temperature for the four different isotopomers of $[(\text{susan}^{6\text{-Me}})\{\text{Fe}^{\text{III}}(\mu\text{-O})(\mu\text{-O}_2)\text{Fe}^{\text{III}}\}](\text{ClO}_4)_2$ indicated by the representation of their central cores and the color scheme used.

We synthesized all four possible $^{18}\text{O}/^{16}\text{O}_2$ -isotopomers as microcrystalline solids. The resonance Raman (rR) and FTIR spectra (Fig. 3) both reveal several ^{18}O -sensitive vibrations, which allow their assignments to the $\{\text{Fe}^{\text{III}}(\mu\text{-O})(\mu\text{-1,2-O}_2)\text{Fe}^{\text{III}}\}$ core (Table 2)^{22,29}. Only slight changes are observed upon dissolution in CH_3CN (Fig. S9). The 831 cm^{-1} band for the two $^{16}\text{O}_2$ -isotopomers is assigned to the $\nu(\text{O-O})$ stretch by isotopic labeling ($\Delta(^{16}\text{O}_2\text{-}^{18}\text{O}_2) = 46 \text{ cm}^{-1}$ consistent with a Hooke's law calculation for a harmonic O-O vibration of 48 cm^{-1}).

The $\nu(\text{O-O})$ stretch of the crystallographically characterized $[(6\text{Me}_2\text{BPP})\{\text{Fe}^{\text{III}}(\mu\text{-O})(\mu\text{-1,2-O}_2)\text{Fe}^{\text{III}}\}(6\text{Me}_2\text{BPP})]$ (A) appears at higher energy at 847 cm^{-1} (Table 2)²². Higher $\nu(\text{O-O})$ stretches were attributed²² to increasing $\angle(\text{Fe-O-O})$ angles¹¹. However, $\angle(\text{Fe-O-O})$ is slightly smaller in A than in our complex (115° vs 117°). Interestingly, the lower $\nu(\text{O-O})$ stretch correlates with a longer O-O distance ($1.432(2) \text{ \AA}$ vs 1.411 \AA) indicating a stronger dependence of $\nu(\text{O-O})$ on $d(\text{O-O})$ than on $\angle(\text{Fe-O-O})$.

$[(\text{susan}^{6\text{-Me}})\{\text{Fe}^{\text{III}}(\mu\text{-O})(\mu\text{-1,2-O}_2)\text{Fe}^{\text{III}}\}]^{2+}$ shows no indication of decay for hours in CH_3CN at $-40 \text{ }^\circ\text{C}$ (Fig. S10). This stability provides the opportunity for the electro- and spectroelectrochemical investigation of a peroxo-diferic complex. $[(\text{susan}^{6\text{-Me}})\{\text{Fe}^{\text{III}}(\mu\text{-O})(\mu\text{-O}_2)\text{Fe}^{\text{III}}\}]^{2+}$ can be reversibly oxidized at $E_{1/2}^{\text{ox}} = 0.55 \text{ V}$ and irreversibly reduced at $E_p^{\text{red}} = -1.28 \text{ V}$ vs Fc^+/Fc (Fig. 4a).

Oxidation to $[(\text{susan}^{6\text{-Me}})\{\text{Fe}(\mu\text{-O})(\mu\text{-1,2-O}_2)\text{Fe}\}]^{3+}$. Coulometric oxidation of $[(\text{susan}^{6\text{-Me}})\{\text{Fe}^{\text{III}}(\mu\text{-O})(\mu\text{-1,2-O}_2)\text{Fe}^{\text{III}}\}]^{2+}$ at 0.68 V vs Fc^+/Fc (1.18 C , 98% of one-electron) in CH_3CN at $-40 \text{ }^\circ\text{C}$ resulted in slight changes of the absorption features

Table 1 Compilation of experimental (on solids or on frozen CH₃CN solutions) and DFT-calculated (shown in italics) ⁵⁷Fe Mössbauer parameters of the complexes reported here and some complexes with the ligands susan and susan^{6-Me} for comparison.

		$\delta/\text{mm s}^{-1}$	$ \Delta E_Q /\text{mm s}^{-1}$	T/K	ref.	
$[(\text{susan}^{6-\text{Me}})\{\text{Fe}^{\text{II}}(\mu\text{-OH})_2\text{Fe}^{\text{II}}\}]^{2+}$	Solid	1.13	2.23	80	a	
$[(\text{susan}^{6-\text{Me}})\{\text{Fe}^{\text{III}}(\mu\text{-O})(\mu\text{-1,2-O}_2)\text{Fe}^{\text{III}}\}]^{2+}$	Solid	0.53	1.69	80	a	
	CH ₃ CN	0.53	1.68	80	a	
	Solid	0.49	1.68	200	a	
	<i>DFT: Fe1</i>	0.58	-1.28		a	
	<i>Fe2</i>	0.53	-1.45			
$[(\text{susan}^{6-\text{Me}})\{\text{Fe}^{\text{III}}(\mu\text{-O})(\mu\text{-1,2-O}_2)\text{Fe}^{\text{IV}}\}]^{3+}$	CH ₃ CN	0.27	+0.57	180	a	
		0.39	-1.29			
	<i>DFT: Fe^{IV}1 Fe^{III}2 configuration</i>	<i>Fe^{IV}1</i>	0.17	+1.00		a
		<i>Fe^{III}2</i>	0.43	-1.21		
	<i>DFT: Fe^{III}1 Fe^{IV}2 configuration</i>	<i>Fe^{IV}2</i>	0.14	+0.67		a
	<i>Fe^{III}1</i>	0.43	-1.00			
$[(\text{susan}^{6-\text{Me}})\{\text{Fe}^{\text{III}}(\mu\text{-O})(\mu\text{-1,2-OOH})\text{Fe}^{\text{III}}\}]^{3+}$	CH ₃ CN	0.49	2.48	80	a	
		0.45	1.37			
	<i>DFT: μ-peroxo-O1 protonated</i>	<i>Fe1</i>	0.54	-1.69		a
		<i>Fe2</i>	0.47	-1.38		
	<i>DFT: μ-peroxo-O2 protonated</i>	<i>Fe1</i>	0.49	+1.05		a
		<i>Fe2</i>	0.48	-2.51		
	<i>DFT: μ-oxo-O3 protonated</i>	<i>Fe1</i>	0.61	-1.74		a
	<i>Fe2</i>	0.56	-0.97			
$[(\text{susan}^{6-\text{Me}})\{\text{Fe}^{\text{III}}(\mu\text{-O})\text{Fe}^{\text{III}}\}]^{2+}$	Solid	0.47	1.38	80	40	
$[(\text{susan})\{\text{Fe}^{\text{III}}(\mu\text{-O})\text{Fe}^{\text{III}}\}]^{2+}$	Solid	0.45	1.68	80	61	
$[(\text{susan})\{\text{Fe}^{\text{III}}(\text{OH})(\mu\text{-O})\text{Fe}^{\text{III}}(\text{OH})\}]^{2+}$	CH ₃ CN	0.45	1.71	80	62	

^aThis work

Quadrupole splittings provided without a sign represent absolute values $|\Delta E_Q|$ obtained from zero-field Mössbauer spectra. The signs provided for $[(\text{susan}^{6-\text{Me}})\{\text{Fe}^{\text{III}}(\mu\text{-O})(\mu\text{-1,2-O}_2)\text{Fe}^{\text{IV}}\}]^{3+}$ were extracted from fits to the magnetic Mössbauer spectra, while signs provided for DFT-calculated values arise from the DFT calculations. Atom labeling scheme related to Fig. 2a.

Table 2 Vibrational (resonance Raman and FTIR) frequencies (cm⁻¹) and isotopic shifts together with some metrical parameters for $[(\text{susan}^{6-\text{Me}})\{\text{Fe}^{\text{III}}(\mu\text{-O})(\mu\text{-1,2-O}_2)\text{Fe}^{\text{III}}\}]^{2+}$ and comparisons to those for A.

	exp. rR	exp. FTIR	A ²²
$\nu(\text{O-O})$ [$\Delta^{18}\text{O}$, $\Delta^{18}\text{O}_2$, $\Delta(^{18}\text{O},^{18}\text{O}_2)$]	831 [0, -46, -46]	831 [0, -46, -46]	847 [-, -33, -]
$\nu_{\text{as}}(\text{Fe-O-Fe})$ [$\Delta^{18}\text{O}$, $\Delta^{18}\text{O}_2$, $\Delta(^{18}\text{O},^{18}\text{O}_2)$]	687 [-35, 0, -37]	686 [-32, 0, -34]	695 [-, -2, -]
$\nu_{\text{s}}(\text{Fe-O-Fe})$ [$\Delta^{18}\text{O}$, $\Delta^{18}\text{O}_2$, $\Delta(^{18}\text{O},^{18}\text{O}_2)$]	≈ 510 [0, -25, -]	n.o.	n.o.
$\nu_{\text{as}}(\text{Fe-O}_2\text{-Fe})$ [$\Delta^{18}\text{O}$, $\Delta^{18}\text{O}_2$, $\Delta(^{18}\text{O},^{18}\text{O}_2)$]	511 (517/506) ^a [-1, -23, -23]	n.o.	n.o.
$\nu_{\text{s}}(\text{Fe-O}_2\text{-Fe})$ [$\Delta^{18}\text{O}$, $\Delta^{18}\text{O}_2$, $\Delta(^{18}\text{O},^{18}\text{O}_2)$]	448 [-1, -23 ^a , -23 ^a]	447 [0, -19, -19]	465 [-, -19, -]
$d(\text{O-O})/\text{\AA}$	1.432(2)		1.41 ^b
$d(\text{Fe}(\mu\text{-O}))/\text{\AA}$	1.875(1)/1.928(1)		1.72 ^b /1.74 ^b
$d(\text{Fe}(\mu\text{-1,2-O}_2))/\text{\AA}$	1.824(1)/1.790(1)		2.07 ^b /2.10 ^b
$\angle(\text{Fe-O-O})^\circ$	116.4(1)/117.5(1)		114.7 ^b /115.3 ^b

^aSplit by Fermi-resonance.

^bThe μ -oxo and μ -1,2-peroxo groups are disordered²² prohibiting a rigid comparison.

(Fig. 4b). Re-reduction at 0.16 V vs Fc⁺/Fc (0.92 C, 76% of one-electron) restored the initial UV-Vis spectrum to ~95% (Fig. 4c and Fig. S11). The lower charge necessary for re-reduction implies some chemical reduction during the coulometric experiments (1 h, Fig. S12).

Chemical oxidation with thianthrenium perchlorate ((thia)ClO₄) generated the UV-Vis spectrum of $[(\text{susan}^{6-\text{Me}})\{\text{Fe}(\mu\text{-O})_2(\mu\text{-O}_2)\text{Fe}\}]^{3+}$ (Fig. 4d) within 10 s. Addition of excess NEt₃ as reductant regenerated the starting spectrum. This emphasizes again the chemical reversibility of the oxidation and indicates the conservation of the μ -oxo, μ -1,2-peroxo motive in the oxidized species.

Characterization of $[(\text{susan}^{6-\text{Me}})\{\text{Fe}(\mu\text{-O})(\mu\text{-1,2-O}_2)\text{Fe}\}]^{3+}$. The EPR spectrum of $[(\text{susan}^{6-\text{Me}})\{\text{Fe}(\mu\text{-O})(\mu\text{-1,2-O}_2)\text{Fe}\}]^{3+}$ (Fig. 5a, S13) shows a broad anisotropic $S_t = 1/2$ signal with $g = (2.272,$

2.152, 2.021). Mössbauer spectroscopy (vide infra) demonstrates that the iron ions remain high-spin ruling out an interpretation as Fe^{III} l.s. species. The severe deviation of $g_{\text{av}} = 2.15$ from 2.0023 and the large g -anisotropy demonstrate a strong contribution of orbital angular momentum and rule out a ligand-centered oxidation to a μ -oxo, μ -1,2-superoxo-Fe^{III}Fe^{III} complex, disclosing a metal-centered oxidation to a μ -oxo, μ -1,2-peroxo-Fe^{IV}Fe^{III} complex with antiferromagnetically coupled Fe^{IV}($S_t = 2$) and Fe^{III}($S_t = 5/2$) ions. The Fe^{IV} h.s. $S_t = 2$ configuration results in $g_1 < 2.0$ by spin-orbit coupling, while the Fe^{III} h.s. is close to isotropic $g_2 \approx 2.00$ ⁴⁶. Projection of the local spins onto the antiferromagnetic $S_t = 1/2$ ground state⁴⁷ results in $g_{\text{av}} > 2.00$ for the $S_t = 1/2$ as observed experimentally³⁹. Despite significant efforts, we were not able to obtain resonance-enhanced Raman features of $[(\text{susan}^{6-\text{Me}})\{\text{Fe}(\mu\text{-O})(\mu\text{-1,2-O}_2)\text{Fe}\}]^{3+}$ by excitation at 647 (15,500), 568 (17,600), and 514 nm (19,500 cm⁻¹) corresponding to the three absorption features of this oxidized complex.

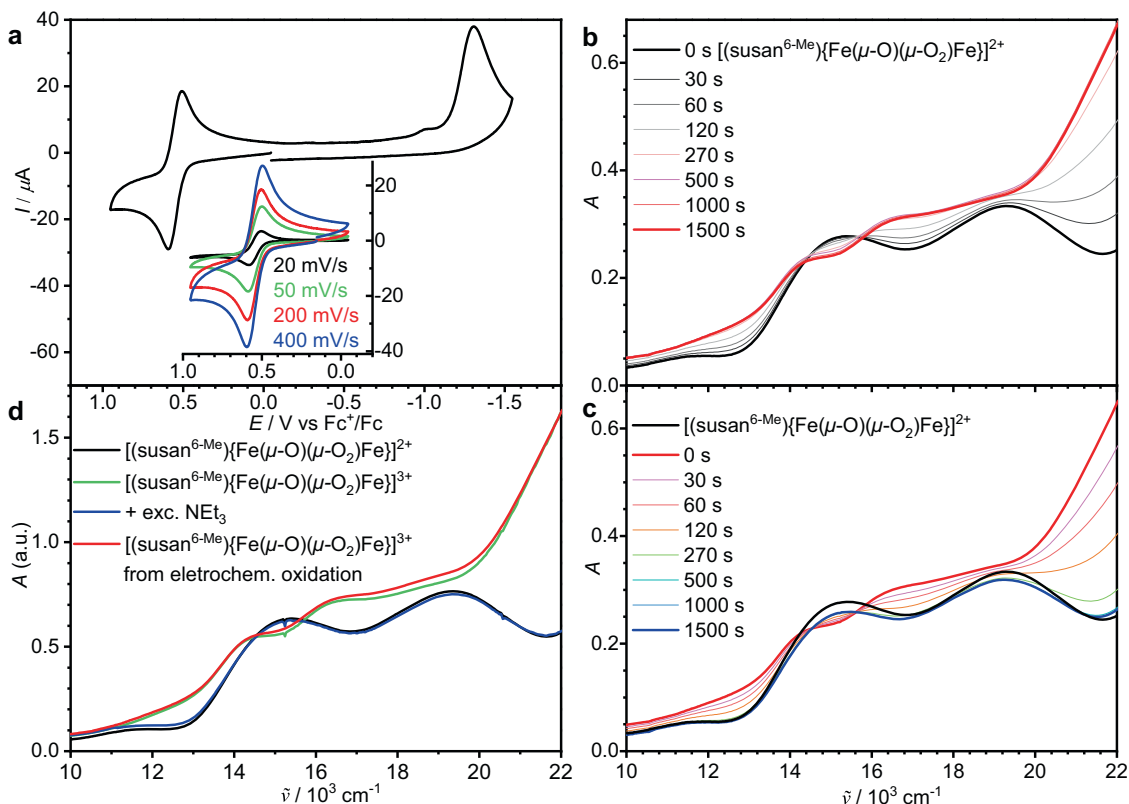


Fig. 4 Electrochemical/spectroelectrochemical characterization of $[(\text{susan}^{6\text{-Me}})\{\text{Fe}^{\text{III}}(\mu\text{-O})(\mu\text{-O}_2)\text{Fe}^{\text{III}}\}](\text{ClO}_4)_2$ and oxidation to $[(\text{susan}^{6\text{-Me}})\{\text{Fe}^{\text{IV}}(\mu\text{-O})(\mu\text{-1,2-O}_2)\text{Fe}^{\text{III}}\}]^{3+}$. **a** Cyclic voltammograms of $[(\text{susan}^{6\text{-Me}})\{\text{Fe}^{\text{III}}(\mu\text{-O})(\mu\text{-O}_2)\text{Fe}^{\text{III}}\}](\text{ClO}_4)_2$ at -20°C in CH_3CN solution (0.2 M $(\text{NBu}_4)\text{PF}_6$) recorded at a GC working electrode. Scan rate 200 mV s^{-1} unless noted otherwise. Spectroelectrochemical measurements at -40°C in CH_3CN (0.2 mM with 0.1 M $(\text{NBu}_4)\text{PF}_6$) during **b** oxidation at $0.68\text{ V vs Fc}^+/\text{Fc}$ and **c** re-reduction at $0.16\text{ V vs Fc}^+/\text{Fc}$. **d** Chemical oxidation with one equivalent (thia)ClO₄ at -60°C in $\text{CH}_3\text{CN}/\text{CH}_2\text{Cl}_2$ (1:1) and re-reduction with excess NEt_3 . The chemically oxidized species (green) almost superimpose with the electrochemically oxidized species (red).

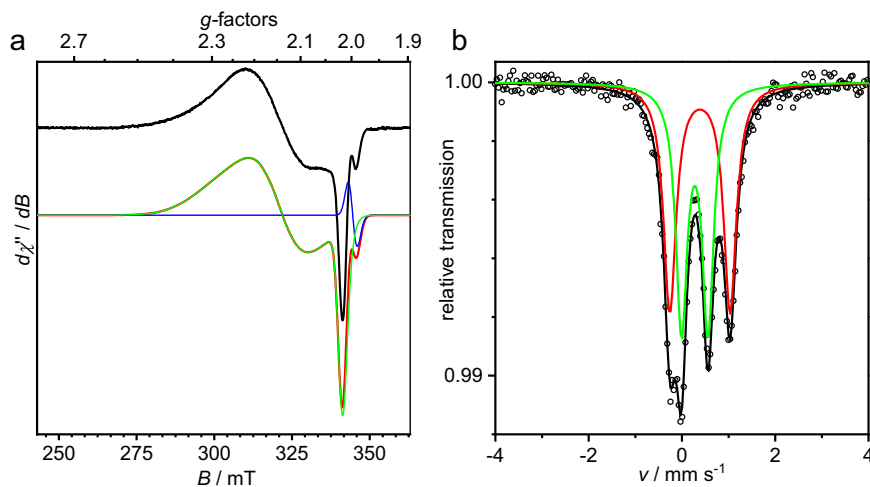


Fig. 5 Spectroscopic characterization of the oxidized complex $[(\text{susan}^{6\text{-Me}})\{\text{Fe}^{\text{IV}}(\mu\text{-O})(\mu\text{-O}_2)\text{Fe}^{\text{III}}\}]^{3+}$. **a** X-band EPR spectrum of chemically oxidized $[(\text{susan}^{6\text{-Me}})\{\text{Fe}^{\text{IV}}(\mu\text{-O})(\mu\text{-O}_2)\text{Fe}^{\text{III}}\}]^{3+}$ in $\approx 0.4\text{ mM}$ CH_3CN solution at 10 K (top, 9.63312 GHz , $80\ \mu\text{W}$ power, 0.75 mT modulation) and its simulation (bottom; simulation red trace, green and blue traces subspectra) with the parameters provided in the text. **b** ^{57}Fe Mössbauer spectra of ^{57}Fe -enriched, chemically oxidized $[(\text{susan}^{6\text{-Me}})\{\text{Fe}^{\text{IV}}(\mu\text{-O})(\mu\text{-O}_2)\text{Fe}^{\text{III}}\}]^{3+}$ in frozen CH_3CN solution at 180 K . The solid lines are simulations with parameters provided in Table 1.

The 180 K Mössbauer spectrum of ^{57}Fe -labeled $[(\text{susan}^{6\text{-Me}})\{\text{Fe}(\mu\text{-O})(\mu\text{-1,2-O}_2)\text{Fe}\}]^{3+}$ (Fig. 5b) exhibits a 4-line spectrum suggesting the presence of two quadrupole doublets. Two different fit models are possible, but considerations explained in the Supplementary

Information (Fig. S14 and S15) strongly favor the model with $\delta_1 = 0.39\text{ mm s}^{-1}/\Delta E_{\text{Q1}} = -1.29\text{ mm s}^{-1}$ and $\delta_2 = 0.27\text{ mm s}^{-1}/\Delta E_{\text{Q2}} = +0.57\text{ mm s}^{-1}$ (Table 1). Interestingly, adding excess NEt_3 as reductant to the oxidized $[(\text{susan}^{6\text{-Me}})\{\text{Fe}(\mu\text{-O})(\mu\text{-1,2-O}_2)\text{Fe}\}]^{3+}$

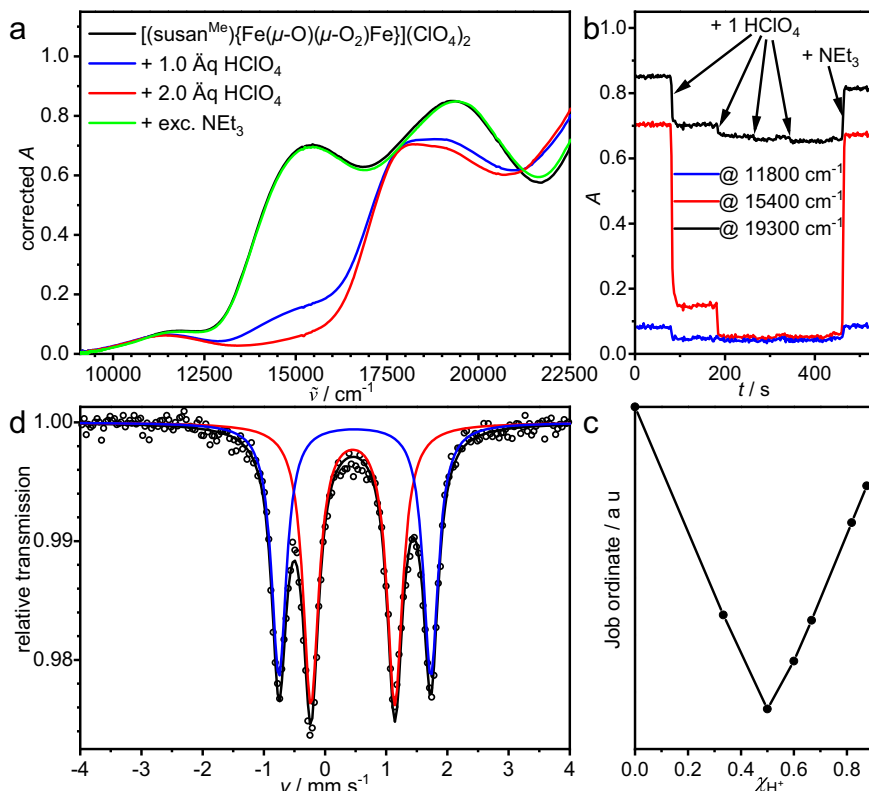


Fig. 6 Protonation of $[(\text{susan}^{6\text{-Me}})\{\text{Fe}^{\text{III}}(\mu\text{-O})(\mu\text{-1,2-O}_2)\text{Fe}^{\text{III}}\}]^{2+}$ and spectroscopic characterization of the protonated complex $[(\text{susan}^{6\text{-Me}})\{\text{Fe}^{\text{III}}(\mu\text{-O})(\mu\text{-1,2-OOH})\text{Fe}^{\text{III}}\}]^{3+}$. **a** UV-Vis spectroscopic characterization of protonation and deprotonation of $[(\text{susan}^{6\text{-Me}})\{\text{Fe}^{\text{III}}(\mu\text{-O})(\mu\text{-1,2-O}_2)\text{Fe}^{\text{III}}\}]^{2+}$ in $\text{CH}_3\text{CN}/\text{CH}_2\text{Cl}_2$ (1:2) at -60°C ($c = 0.77\text{ mM}$). **b** Selected time traces for the protonation/deprotonation in **a**. **c** Job-plot analysis at $15,400\text{ cm}^{-1}$ of the protonation in **a**. **d** ^{57}Fe Mössbauer spectrum of a frozen solution of $[(\text{susan}^{6\text{-Me}})\{\text{Fe}^{\text{III}}(\mu\text{-O})(\mu\text{-1,2-OOH})\text{Fe}^{\text{III}}\}]^{3+}$ at 80 K generated by treating $[(\text{susan}^{6\text{-Me}})\{\text{Fe}^{\text{III}}(\mu\text{-O})(\mu\text{-1,2-O}_2)\text{Fe}^{\text{III}}\}]^{2+}$ with 1.5 equivalents HClO_4 in CH_3CN at -40°C . The solid lines are simulations with parameters provided in Table 1.

restores the Mössbauer spectrum of the starting complex $[(\text{susan}^{6\text{-Me}})\{\text{Fe}^{\text{III}}(\mu\text{-O})(\mu\text{-O}_2)\text{Fe}^{\text{III}}\}]^{2+}$ (Fig. S16) confirming the chemical reversibility.

The decrease of the isomer shift from 0.53 mm s^{-1} of the starting complex to 0.27 and 0.39 mm s^{-1} confirms a mainly metal-centered oxidation to a high-valent $\mu\text{-1,2-peroxo}$ complex with both Fe^{III} ions involved resulting in a mixed-valence $\text{Fe}^{\text{IV}}\text{Fe}^{\text{III}}$ species. In the Robin-and-Day classification for mixed-valence systems⁴⁸, class I implies no interaction (ruled out by the coupled $S_1 = 1/2$ spin ground state) while class III stands for quantum-mechanically delocalized states. In class II systems, two different states exist that correspond roughly to the excess electron localized on the one or the other metal ion. Between these two states is an energy barrier and there can be temperature-dependent and light-induced mechanisms to transfer the excess electron from the reduced to the oxidized metal ion. In symmetric cases, the two states are energetically degenerate while the asymmetry observed here results in an energy difference between these two states (Fig. S17). The two quadrupole doublets can arise from one of these states populated exclusively up to 180 K or from an electron hopping between these two states at a rate faster than the Mössbauer timescale (10^{-7} s). To differentiate between these two possibilities, we recorded Mössbauer spectra at lower temperatures (Fig. S18). Unfortunately, the spectra broadened with decreasing temperature due to a relaxation process that is fast relative to the Mössbauer timescale at only 180 K . The origin cannot only arise from a decrease of the electron hopping rate but also from paramagnetic effects. DFT calculations (Supplementary Information) provided two localized configurations $\text{Fe}^{\text{IV}}\text{Fe}^{\text{III}}_2$ and $\text{Fe}^{\text{III}}\text{Fe}^{\text{IV}}_2$ that both reproduce

the isomer shift decrease of both iron ions (Table 1) and hence confirm the assignment to class II. However, although these DFT calculations provided $\text{Fe}^{\text{IV}}\text{Fe}^{\text{III}}_2$ being lower in energy by $\approx 820\text{ cm}^{-1}$, more advanced MO calculations are required to obtain further insight that are beyond this study.

Protonation to $[(\text{susan}^{6\text{-Me}})\{\text{Fe}^{\text{III}}(\mu\text{-O})(\mu\text{-1,2-OOH})\text{Fe}^{\text{III}}\}]^{3+}$. Treatment of a solution of $[(\text{susan}^{6\text{-Me}})\{\text{Fe}^{\text{III}}(\mu\text{-O})(\mu\text{-1,2-O}_2)\text{Fe}^{\text{III}}\}]^{2+}$ with HClO_4 at -60°C resulted in the loss of the $15,400\text{ cm}^{-1}$ band while the $11,800$ and $19,300\text{ cm}^{-1}$ bands are only slightly affected (Fig. 6a, b). A Job plot analysis^{49,50} (Fig. 6c) provided a 1:1 stoichiometry for the reaction between the $\mu\text{-1,2-peroxo}$ complex and H^+ . Adding NEt_3 as a base restores the initial spectrum (Fig. 6a) showing the reversibility of this protonation.

Characterization of $[(\text{susan}^{6\text{-Me}})\{\text{Fe}^{\text{III}}(\mu\text{-O})(\mu\text{-1,2-OOH})\text{Fe}^{\text{III}}\}]^{3+}$. The disappearance of the $\mu\text{-1,2-peroxo} \rightarrow \text{Fe}^{\text{III}}$ LMCT at $15,400\text{ cm}^{-1}$, while the $\mu\text{-oxo} \rightarrow \text{Fe}^{\text{III}}$ LMCT around $19,000\text{ cm}^{-1}$ persists, is consistent with protonation of the $\mu\text{-1,2-peroxo}$ ligand. In contrast, protonation of complex A to the $\mu\text{-hydroxo},\mu\text{-1,2-peroxo}$ complex is accompanied by a shift of the $\mu\text{-1,2-peroxo} \rightarrow \text{Fe}^{\text{III}}$ LMCT from $17,300\text{ cm}^{-1}$ to $15,500\text{ cm}^{-1}$ ¹²². A similar shift was observed using a linear N_4 ligand³⁶. Moreover, the persistence of the weaker feature at $11,800\text{ cm}^{-1}$ assigns this to a $\mu\text{-oxo} \rightarrow \text{Fe}^{\text{III}}$ LMCT. However, the absence of a $\mu\text{-1,2-hydroperoxo} \rightarrow \text{Fe}^{\text{III}}$ LMCT prohibits excitation for rR spectra at 647 nm ($15,500\text{ cm}^{-1}$). Neither were resonance-enhanced vibrations observed by excitation at 568

(17,600) and 514 nm (19,500 cm⁻¹) close to the μ -oxo \rightarrow Fe^{III} LMCT (Fig. 6a).

The Mössbauer spectrum provided two quadrupole doublets with $\delta_1 = 0.49 / |\Delta E_Q|_1 = 2.48$ mm s⁻¹ and $\delta_2 = 0.45 / |\Delta E_Q|_2 = 1.37$ mm s⁻¹ (Fig. 6d). Since the parent [(susan^{6-Me}){Fe^{III}(μ -O)(μ -1,2-O₂)Fe^{III}}]²⁺ exhibits only one quadrupole doublet despite the significant differences in its two coordination sites (vide supra) requires a different source of asymmetry for the protonated species to explain its two strongly differing quadrupole doublets. This rules out a μ -1,1-hydroperoxo-bridge, while a μ -1,2-hydroperoxo-bridge provides the different source of asymmetry as the protonated site becomes much less charge-donating. Although a terminally bound hydroperoxo-ligand would be in-line with the absence of a μ -1,2-peroxo \rightarrow Fe^{III} LMCT and two quadrupole doublets, the persistence of the μ -oxo \rightarrow Fe^{III} LMCTs around 19,000 and 11,800 cm⁻¹ strongly favors a doubly-bridged structure of almost the same α (Fe^{III}(μ -O)-Fe^{III}) angle hence ruling out an almost linear {Fe^{III}(OOH)(μ -O)Fe^{III}X} core^{38,40} that is also inaccessible with the ligand susan^{6-Me} (vide infra).

The formation of a μ -1,2-hydroperoxo-bridged complex is supported by DFT calculations (Supplementary Information). Geometry optimizations were achieved for three different tautomers with protonation of the μ -peroxo-O1 being 1200 cm⁻¹ higher in energy. Although the μ -hydroxo species (protonation of the μ -oxo-O3) seems energetically feasible, its isomer shifts are even higher than for the starting peroxo complex (Table 1). In contrast, protonation at the μ -peroxo-O2 decreases the isomer shifts as experimentally observed. Thus, the μ -1,2-hydroperoxo ligand is most likely protonated at O2.

Further reactivity studies. The straightforward fast protonation of [(susan^{6-Me}){Fe^{III}(μ -O)(μ -O₂)Fe^{III}}]²⁺ with HClO₄ demonstrates the nucleophilic character of the μ -1,2-peroxo ligand. On the other hand, the reaction of [(susan^{6-Me}){Fe^{III}(μ -O)(μ -O₂)Fe^{III}}]²⁺ with 2-phenylpropanal as a typical substrate to evaluate the nucleophilic character of peroxo ligands^{51,52} is slow in CH₃CN at -5 °C (Fig. S19). However, the formation of roughly one equivalent of acetophenone by performing this reaction on a preparative scale for 5 days supports the slow nucleophilic reactivity of the μ -1,2-peroxo ligand.

The electrophilic character was not only evaluated for [(susan^{6-Me}){Fe^{III}(μ -O)(μ -O₂)Fe^{III}}]²⁺ but also for the oxidized μ -1,2-peroxo-Fe^{IV}Fe^{III} and the protonated μ -1,2-hydroperoxo-diferric species as both oxidation and protonation should increase the electrophilic character. This is already reflected in the different stabilities of these species (Fig. S10). As [(susan^{6-Me}){Fe^{III}(μ -O)(μ -1,2-O₂)Fe^{III}}]²⁺ shows no indication of decay for hours in CH₃CN at -40 °C, oxidized [(susan^{6-Me}){Fe^{IV}(μ -O)(μ -O₂)Fe^{III}}]³⁺ and protonated [(susan^{6-Me}){Fe^{III}(μ -O)(μ -1,2-OOH)Fe^{III}}]³⁺ decay with half-lives of $\tau_{1/2} \approx 90$ min $\tau_{1/2} \approx 11$ min, respectively. Therefore, the clean characterization of the latter two species required lower temperatures of -60 °C and hence addition of a certain amount of CH₂Cl₂.

The electrophilic character of the three complexes were initially investigated using 9,10-dihydroanthracene (DHA) and PPh₃ as typical substrates for HAT and OAT, respectively. The reactions with [(susan^{6-Me}){Fe^{III}(μ -O)(μ -O₂)Fe^{III}}]²⁺ were performed in CH₃CN at -40 °C, while that with [(susan^{6-Me}){Fe^{IV}(μ -O)(μ -O₂)Fe^{III}}]³⁺ and [(susan^{6-Me}){Fe^{III}(μ -O)(μ -1,2-OOH)Fe^{III}}]³⁺ at -60 °C in CH₃CN/CH₂Cl₂ mixtures (vide supra). The parent [(susan^{6-Me}){Fe^{III}(μ -O)(μ -O₂)Fe^{III}}]²⁺ showed no reactivity towards DHA and PPh₃ (Figs. S20, S21). The oxidized [(susan^{6-Me}){Fe^{IV}(μ -O)(μ -O₂)Fe^{III}}]³⁺ also showed no reactivity towards DHA (Fig. S22), while the reaction with PPh₃ resulted in the reoccurrence of the UV-Vis signature of the parent

[(susan^{6-Me}){Fe^{III}(μ -O)(μ -O₂)Fe^{III}}]²⁺ (Fig. S23). The reformation of the μ -1,2-peroxo \rightarrow Fe^{III} LMCT excludes an OAT reactivity between [(susan^{6-Me}){Fe^{IV}(μ -O)(μ -O₂)Fe^{III}}]³⁺ and PPh₃ but suggests an oxidation of PPh₃⁵³ by [(susan^{6-Me}){Fe^{IV}(μ -O)(μ -O₂)Fe^{III}}]³⁺. Analogous observations were made with the protonated [(susan^{6-Me}){Fe^{III}(μ -O)(μ -1,2-OOH)Fe^{III}}]³⁺ that showed no reactivity with DHA (Fig. S24) and with PPh₃ the partial recovery of the UV-Vis signature of the parent [(susan^{6-Me}){Fe^{III}(μ -O)(μ -O₂)Fe^{III}}]²⁺ (Fig. S25). Again, the reformation of the μ -1,2-peroxo \rightarrow Fe^{III} LMCT excludes an OAT reactivity between [(susan^{6-Me}){Fe^{III}(μ -O)(μ -1,2-OOH)Fe^{III}}]³⁺ and PPh₃. The partial recovery of [(susan^{6-Me}){Fe^{III}(μ -O)(μ -O₂)Fe^{III}}]²⁺ indicates a protonation equilibrium between PPh₃⁵⁴ and [(susan^{6-Me}){Fe^{III}(μ -O)(μ -1,2-OOH)Fe^{III}}]³⁺.

As it is not surprising^{35,55} that [(susan^{6-Me}){Fe^{III}(μ -O)(μ -O₂)Fe^{III}}]²⁺ exhibits no electrophilic reactivity against DHA, the non-reactivity of both oxidized [(susan^{6-Me}){Fe^{IV}(μ -O)(μ -O₂)Fe^{III}}]³⁺ and protonated [(susan^{6-Me}){Fe^{III}(μ -O)(μ -1,2-OOH)Fe^{III}}]³⁺ is quite surprising. To further understand this non-reactivity, we determined the BDFE(OH)_{CH₃CN} of [(susan^{6-Me}){Fe^{III}(μ -O)(μ -1,2-OOH)Fe^{III}}]³⁺. In this respect, we determined the pK_a of [(susan^{6-Me}){Fe^{III}(μ -O)(μ -1,2-OOH)Fe^{III}}]³⁺ in CH₃CN that provided 9.5 ± 0.1 (Fig. S26). Using the typical square scheme (Fig. 7a) and the Bordwell relation Eq. (1)⁵⁶⁻⁵⁸

$$\text{BDFE(O-H)}_{\text{CH}_3\text{CN}} = 1.37 \text{ p}K_a + 23.06 E^{\text{O}^{\cdot}} + 52.6 \text{ kcal mol}^{-1} \quad (1)$$

provided BDFE(O-H)_{CH₃CN} = 78 ± 2 kcal mol⁻¹. This means that [(susan^{6-Me}){Fe^{IV}(μ -O)(μ -O₂)Fe^{III}}]³⁺ should be capable as oxidant for HAT for substrates with a lower BDFE(X-H)_{CH₃CN}. The BDE(C-H) of DHA is 76.3 kcal mol⁻¹⁵⁹. However, the intrinsic difference between BDFE and BDE⁵⁷, the temperature-dependence of BDFE especially for transition metal complexes, and the experimental error explain the non-reactivity of [(susan^{6-Me}){Fe^{IV}(μ -O)(μ -O₂)Fe^{III}}]³⁺ with DHA. In this respect, TEMPOH should be a suitable HAT substrate with BDFE(O-H)_{CH₃CN} = 66.5 kcal mol⁻¹ and BDE(O-H) = 70.6 kcal mol⁻¹⁵⁷ especially for [(susan^{6-Me}){Fe^{IV}(μ -O)(μ -O₂)Fe^{III}}]³⁺.

The parent [(susan^{6-Me}){Fe^{III}(μ -O)(μ -O₂)Fe^{III}}]²⁺ showed no reactivity with TEMPOH (Fig. S27), which is in-line that this one-electron reduced species [(susan^{6-Me}){Fe^{III}(μ -O)(μ -O₂)Fe^{III}}]²⁺ should have a driving force for HAT significantly lower than 78 kcal mol⁻¹ of [(susan^{6-Me}){Fe^{IV}(μ -O)(μ -O₂)Fe^{III}}]³⁺. The reaction of protonated [(susan^{6-Me}){Fe^{III}(μ -O)(μ -1,2-OOH)Fe^{III}}]³⁺ with TEMPOH resulted in the reoccurrence of the UV-Vis signature of the parent [(susan^{6-Me}){Fe^{III}(μ -O)(μ -O₂)Fe^{III}}]²⁺ (Fig. S28). The reformation of the parent μ -1,2-peroxo-diferric complex excludes a HAT reactivity between [(susan^{6-Me}){Fe^{III}(μ -O)(μ -1,2-OOH)Fe^{III}}]³⁺ and TEMPOH and suggests a protonation of TEMPOH⁶⁰. The reaction of [(susan^{6-Me}){Fe^{IV}(μ -O)(μ -O₂)Fe^{III}}]³⁺ with TEMPOH resulted in the reoccurrence of the UV-Vis signature of the parent [(susan^{6-Me}){Fe^{III}(μ -O)(μ -O₂)Fe^{III}}]²⁺ (Fig. S29). This is in-line with HAT from TEMPOH to [(susan^{6-Me}){Fe^{IV}(μ -O)(μ -O₂)Fe^{III}}]³⁺ resulting in [(susan^{6-Me}){Fe^{III}(μ -O)(μ -1,2-OOH)Fe^{III}}]³⁺ that reacts again by protonation of excess TEMPOH to [(susan^{6-Me}){Fe^{III}(μ -O)(μ -O₂)Fe^{III}}]²⁺.

Thus, only the oxidized [(susan^{6-Me}){Fe^{IV}(μ -O)(μ -O₂)Fe^{III}}]³⁺ is capable for HAT from TEMPOH corroborated by the BDFE while the parent [(susan^{6-Me}){Fe^{III}(μ -O)(μ -O₂)Fe^{III}}]²⁺ and the protonated [(susan^{6-Me}){Fe^{III}(μ -O)(μ -1,2-OOH)Fe^{III}}]³⁺ does not exhibit enough electrophilic character. However, [(susan^{6-Me}){Fe^{III}(μ -O)(μ -O₂)Fe^{III}}]²⁺ that shows no decay at -40 °C exhibits a change in the UV-Vis spectra at room temperature with the formation of the typical signature of complexes with a {Fe^{III}X(μ -O)Fe^{III}X} core³⁸ without the observation of intermediates

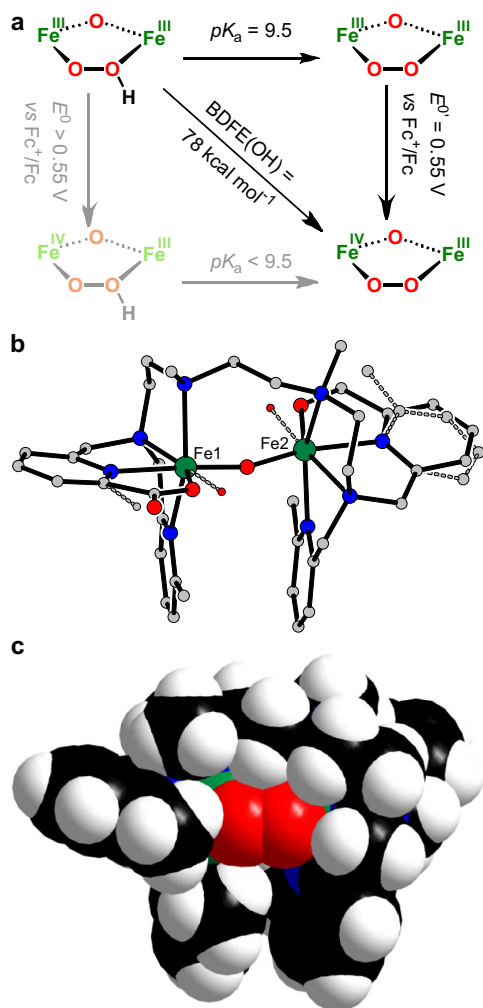


Fig. 7 Reactivity studies. **a** Square scheme showing the PCET thermochemistry of the decay product of $[(\text{susan}^{6-\text{Me}})\{\text{Fe}^{\text{III}}(\mu\text{-O})(\mu\text{-1,2-OOH})\text{Fe}^{\text{III}}\}]^{3+}$ in CH_3CN . **b** Molecular structure of the decay product of $[(\text{susan}^{6-\text{Me}})\{\text{Fe}^{\text{III}}(\mu\text{-O})(\mu\text{-1,2-O}_2)\text{Fe}^{\text{III}}\}]^{2+}$ including the ligand disorders (please see also Supplementary Fig. 1c): at Fe1 80% carboxylate and 20% hydroxide (shown with dotted lines), at Fe2 35% benzylalcoholato and 65% hydroxide (shown with dotted lines). **c** Space-filling model of $[(\text{susan}^{6-\text{Me}})\{\text{Fe}^{\text{III}}(\mu\text{-O})(\mu\text{-1,2-O}_2)\text{Fe}^{\text{III}}\}]^{2+}$ to illustrate the encapsulation of the peroxo ligand by a CH_2 group (right Fe) and a 6-methyl group (left Fe).

accompanied by deposition of an inhomogeneous solid and a few single-crystals. The crystallographic analysis provided the structure of the decay product (Fig. 7b) based on $[(\text{susan}^{6-\text{Me}})\{\text{Fe}^{\text{III}}(\text{OH})(\mu\text{-O})\text{Fe}^{\text{III}}(\text{OH})\}]^{2+61}$ with a disorder of the coordinated OH^- ligands, which could be resolved to coordination of oxidized 6-methyl groups. At Fe1, only 20% is OH^- while 80% is a carboxylate while at Fe2, 65% is OH^- and 35% consists of a benzylalcoholato donor. NMR spectroscopy of the demetallated bulk decay product shows the formation of more than one product but a significant signal at 173.4 ppm for a benzoic acid group in the ^{13}C NMR spectrum indicates that the hydroxylation of the 6-methyl group is not only a minor reaction path.

Discussion

To mimic dinuclear active sites of metalloenzymes, we have developed a dinucleating ligand system with varying terminal donors^{38,39}. With the ligand *susan*, we obtained in straightforward reactions a series of μ -oxo-diferric complexes $\{\text{Fe}^{\text{III}}\text{X}(\mu\text{-O})$

$\text{Fe}^{\text{III}}\text{X}\}$ bearing anionic exogenous ligands $\text{X}^{37,39,45,61}$. The complex with hydroxides, $[(\text{susan})\{\text{Fe}^{\text{III}}(\text{OH})(\mu\text{-O})\text{Fe}^{\text{III}}(\text{OH})\}]^{2+}$, catalyzes the oxidation of CH_3OH with H_2O_2 to HCHO ⁶². We could observe the μ -1,2-peroxy intermediate $[(\text{susan})\{\text{Fe}^{\text{III}}(\mu\text{-O})(\mu\text{-1,2-O}_2)\text{Fe}^{\text{III}}\}]^{2+}$. However, the temperature-dependencies ruled out this μ -1,2-peroxy intermediate to be the active species indicating the conversion to a high-valent active species. This conversion is faster in the presence of a proton suggesting a transient μ -1,2-hydroperoxy species.

In contrast, formation of μ -oxo-diferric complexes with *susan*^{6-Me} was not possible under identical aerobic conditions. Only the small ligand F^- with H_2O_2 as oxidant allowed the isolation of $[(\text{susan}^{6-\text{Me}})\{\text{Fe}^{\text{III}}\text{F}(\mu\text{-O})\text{Fe}^{\text{III}}\text{F}\}]^{2+40}$. Its comparison to $[(\text{susan})\{\text{Fe}^{\text{III}}\text{F}(\mu\text{-O})\text{Fe}^{\text{III}}\text{F}\}]^{2+}$ showed a steric repulsion between the 6-methyl group and the terminal F^- ligand in *cis*-position, which explains the inaccessibility of *susan*^{6-Me} complexes with larger terminal ligands as Cl^- or OAc^- that are easily accessible with *susan*. Thus, the μ -oxo-bridged core $\{\text{Fe}^{\text{III}}\text{X}(\mu\text{-O})\text{Fe}^{\text{III}}\text{X}\}$ is not the thermodynamic sink for *susan*^{6-Me} as it is for *susan*. Moreover, the steric repulsion of the 6-methyl group enforces longer $\text{Fe-N}^{6-\text{Me-py}}$ than Fe-NPY bonds^{63–68}, and hence a lower electron donation. This results in an anodic shift of +250 mV making Fe^{IV} less accessible with *susan*^{6-Me} than with *susan*.

In this respect, we thought that *susan*^{6-Me} should be able to stabilize a μ -1,2-peroxy complex $\{\text{Fe}^{\text{III}}(\mu\text{-O})(\mu\text{-1,2-O}_2)\text{Fe}^{\text{III}}\}$ that is with *susan* only a reactive intermediate decaying via a high-valent Fe^{IV} species to its thermodynamic sink $\{\text{Fe}^{\text{III}}\text{X}(\mu\text{-O})\text{Fe}^{\text{III}}\text{X}\}$. In contrast, with *susan*^{6-Me} not only this thermodynamic driving force is absent but Fe^{IV} is also less accessible. Indeed, we could present here the synthesis and characterization of the stable μ -1,2-peroxy complex $[(\text{susan}^{6-\text{Me}})\{\text{Fe}^{\text{III}}(\mu\text{-O})(\mu\text{-1,2-O}_2)\text{Fe}^{\text{III}}\}]^{2+}$. Inspection of the space-filling model (Fig. 7c) shows that the μ -1,2-peroxy ligand is even further stabilized by a better encapsulation with the 6-methyl group of *susan*^{6-Me} (left peroxo-oxygen atom in Fig. 7c) that would be absent with *susan*. This ligand encapsulation also explains the slower nucleophilic reactivity of the μ -1,2-peroxy ligand for the organic substrate 2-phenylpropanal than for the small H^+ .

Although *susan*^{6-Me} is less suited for stabilization of Fe^{IV} than *susan*, the principal accessibility of Fe^{IV} with *susan*^{6-Me} is demonstrated by the reversible oxidation to $[(\text{susan}^{6-\text{Me}})\{\text{Fe}^{\text{IV}}(\mu\text{-O})(\mu\text{-1,2-O}_2)\text{Fe}^{\text{III}}\}]^{3+}$, which is stabilized by the additional highly covalent μ -1,2-peroxy ligand. It is interesting to note, that this high-valent μ -1,2-peroxy species stores one oxidation-equivalent more than intermediate **Q** of sMMO. Comparing the $\text{Fe}^{\text{IV}}\text{Fe}^{\text{III}}/\text{Fe}^{\text{III}}\text{Fe}^{\text{III}}$ redox potential of $E_{1/2} = 0.55$ V to 0.41 V vs Fc^+/ Fc for the analogous redox couple of $[(\text{tpa}^{6-\text{Me}})\{\text{Fe}^{\text{III}}(\mu\text{-O})_2\text{Fe}^{\text{III}}\}]^{2+69}$ shows only a slightly lower electron-donating character of the μ -1,2-peroxy-bridge than a μ -oxo-bridge.

We could further demonstrate the reversible protonation to the μ -1,2-hydroperoxy-diferric complex $[(\text{susan}^{6-\text{Me}})\{\text{Fe}^{\text{III}}(\mu\text{-O})(\mu\text{-1,2-OOH})\text{Fe}^{\text{III}}\}]^{3+}$. Generally, protonation of a Fe-coordinated peroxo ligand is regarded to enhance its reactivity, e. g. protonation of the *cis*- μ -1,2-peroxy intermediate **P** of sMMO was proposed to promote the conversion to intermediate **Q**¹¹. The relatively high stability of the μ -1,2-hydroperoxy complex $[(\text{susan}^{6-\text{Me}})\{\text{Fe}^{\text{III}}(\mu\text{-O})(\mu\text{-1,2-OOH})\text{Fe}^{\text{III}}\}]^{3+}$ (no decay at -60°C , $\tau_{1/2} \approx 11$ min at -40°C) is thus remarkable and must owe its origin to a low stabilization of the Fe^{IV} conversion product by *susan*^{6-Me}.

In contrast to $[(\text{susan}^{6-\text{Me}})\{\text{Fe}^{\text{III}}(\mu\text{-O})(\mu\text{-1,2-O}_2)\text{Fe}^{\text{III}}\}]^{2+}$, the μ -1,2-peroxy complex **A** is protonated at the μ -oxo-bridge forming a $\{\text{Fe}^{\text{III}}(\mu\text{-1,2-O}_2)(\mu\text{-OH})\text{Fe}^{\text{III}}\}$ species²² indicating different nucleophilicities. The nucleophilic character of a ligand should increase with less electron donation to the Fe^{III} ions, i. e. less covalent, longer bonds. But for **A**, the $\text{Fe}^{\text{III}}\text{-}\mu\text{-O}^{\text{oxo}}$ bonds are shorter than for $[(\text{susan}^{6-\text{Me}})\{\text{Fe}^{\text{III}}(\mu\text{-O})(\mu\text{-1,2-O}_2)\text{Fe}^{\text{III}}\}]^{2+}$

(1.72/1.74 Å vs 1.82/1.89 Å), whereas the situation is reversed for the Fe^{III}-μ-O^{peroxo} bonds (2.07/2.10 Å vs 1.88/1.93 Å). This structural argumentation is in contrast to the experimentally determined protonation sites. However, the disorder of the μ-oxo/μ-1,2-peroxo ligands in **A** questions the significance of this comparison. Moreover, as protonation should occur at a p^π orbital and a Fe-O bond consists of σ- and π-bonding, a pure structural analysis does not need to provide the answer for the reactivity.

Thus, spectroscopic markers might provide a better correlation to the nucleophilic character of the peroxo group than structural parameters. Solomon and coworkers proposed to extract the donor strength of a given ligand from the integrated absorption intensities of all CT transitions associated with this ligand⁷⁰. Here, the π-charge donation from the peroxo π*_π donor orbital into the Fe 3d_π acceptor orbitals should be extractable from the prominent μ-1,2-peroxo → Fe LMCTs. Complex **A** exhibits this μ-1,2-peroxo → Fe^{III} LMCT with ε = 1500 M⁻¹ cm⁻¹ and a much less intense μ-oxo → Fe^{III} LMCT. In contrast, the μ-oxo → Fe^{III} LMCT in [(susan^{6-Me}){Fe^{III}(μ-O)(μ-1,2-O₂)Fe^{III}}]²⁺ is more intense (ε = 1180 M⁻¹ cm⁻¹) than the μ-peroxo → Fe^{III} LMCT (ε = 1000 M⁻¹ cm⁻¹). Note that also the integrated absorption intensity is smaller in the susan^{6-Me} complex than in **A** for the μ-1,2-peroxo → Fe^{III} LMCT indicating - without the intention of a quantitative analysis - less charge-donation and hence more nucleophilic character of the μ-1,2-peroxo ligand. This UV-Vis spectroscopic argumentation is supported by a comparison of the vibrational signature in the rR spectra. Interestingly, the strongest difference is observed for the ν_s(Fe-O₂-Fe), which are at 465 and 448 cm⁻¹ for **A** and [(susan^{6-Me}){Fe^{III}(μ-O)(μ-1,2-O₂)Fe^{III}}]²⁺, respectively, indicative for less covalent Fe^{III}-μ-O^{peroxo} bonds and hence a higher nucleophilicity of the μ-1,2-peroxo ligand in [(susan^{6-Me}){Fe^{III}(μ-O)(μ-1,2-O₂)Fe^{III}}]²⁺.

The study of the electrophilic reactivity demonstrated only a low electrophilic character of the parent μ-1,2-peroxo-Fe^{III}Fe^{III} complex that is not unexpected for such complexes^{35,55}. Interestingly, also protonation to the μ-1,2-hydroperoxo-Fe^{III}Fe^{III} species turned out to be not sufficient to increase the electrophilic character for HAT with substrates of weak to modest BDE (TEMPOH and DHA). Only the oxidized μ-1,2-peroxo-Fe^{IV}Fe^{III} species reacts with the relatively weak substrate TEMPOH. The determination of the pK_a = 9.5 ± 0.1 and the bond dissociation free energy BDFE(O-H)_{CH₃CN} = 78 ± 2 kcal mol⁻¹ of the protonated μ-1,2-hydroperoxo-Fe^{III}Fe^{III} species quantifies this low electrophilic character even of the oxidized μ-1,2-peroxo-Fe^{IV}-Fe^{III} species. In this respect, the intramolecular C-H activation of preorganized 6-methyl pyridine groups to benzylalcoholato and carboxylato donors by the parent μ-1,2-peroxo-Fe^{III}Fe^{III} complex is remarkable. Considering that this complex does not react with TEMPOH (BDE(O-H) = 70.6 kcal mol⁻¹) and using the BDE(C-H) = 90 kcal mol⁻¹⁵⁹ of the methyl group of toluene as an approximation for the BDE(C-H) of the 6-methyl groups of the coordinated pyridines, HAT should not occur via the bridging μ-1,2-peroxo-ligand. This indicates that this intramolecular reaction requires the conversion of the μ-1,2-peroxo-diferric core to a more reactive high-valent species as already postulated for the CH₃OH oxidation⁶² of the analogous μ-1,2-peroxo-diferric complex of susan (*vide supra*).

[(susan^{6-Me}){Fe^{III}(μ-O)(μ-1,2-OOH)Fe^{III}}]³⁺ is an μ-1,2-hydroperoxo model complex and provides spectroscopic signatures for the assignment of postulated hydroperoxo intermediates in diiron enzymes: Upon protonation, the prominent μ-1,2-peroxo → Fe^{III} LMCT around 14,000–16,000 cm⁻¹ disappears and the isomer shift decreases. The presence of an μ-oxo-bridge is indicated by the typical μ-oxo → Fe^{III} LMCTs around 12,000 and 19,000 cm⁻¹ and large values of |ΔE_Q| ≥ 1.3 mm s⁻¹. The best signature to

differentiate between a μ-1,1-hydroperoxo and a μ-1,2-hydroperoxo is the appearance of two strongly differing quadrupole doublets for the latter due to the strongly differing donation abilities of the two μ-1,2-hydroperoxo-oxygen atoms.

The protonation of [(susan^{6-Me}){Fe^{III}(μ-O)(μ-1,2-O₂)Fe^{III}}]²⁺ to [(susan^{6-Me}){Fe^{III}(μ-O)(μ-1,2-OOH)Fe^{III}}]³⁺ reflect the UV-Vis-NIR and Mössbauer spectroscopic differences between **P** and the more reactive **P'** intermediates in non-heme diiron enzymes^{2,15,16,20}. For the latter, a μ-1,2-hydroperoxo structure has been suggested, which is thus strongly supported by the results of this study.

The diferrous form of AurF exhibits one quadrupole doublet demonstrating structurally rather similar iron places¹². Reaction with O₂ provides a diferric species that lacks the typical μ-1,2-peroxo → Fe^{III} LMCT around 14,000 cm⁻¹. The Mössbauer spectrum contains two quite different quadrupole doublets with δ₁ = 0.54, ΔE_{Q1} = 0.66 mm s⁻¹ and δ₂ = 0.61, ΔE_{Q2} = 0.35 mm s^{-112,13}. This coupled with the low values of |ΔE_Q| and a lack of the μ-1,2-peroxo → Fe^{III} LMCT leads us to suggest the formulation of the **P'**-type intermediate in AurF as a {Fe^{III}(μ-1,2-hydroperoxo)Fe^{III}} core without a μ-oxo-bridge, which also supports a recent proposal¹⁵.

Methods

Synthesis of [(susan^{6-Me}){Fe^{II}(μ-OH)₂Fe^{II}}](ClO₄)₂·H₂O. A solution of susan^{6-Me} (595 mg, 1.00 mmol) in MeOH (25 mL) was added to a solution of Fe(ClO₄)₂·6H₂O (726 mg, 2.00 mmol, 2.0 equiv) in MeOH (20 mL). This yellow solution was stirred at room temperature for 10 min followed by an addition of a 25% aqueous solution of ammonia (0.16 mL, 2.1 mmol, 2.1 equiv) resulting in a slight intensity increase of the yellow color. Yellow crystals of [(susan^{6-Me}){Fe^{II}(μ-OH)₂Fe^{II}}](ClO₄)₂·MeOH precipitated at 0 °C, which were filtered off, washed three times with water, a small amount of cold MeOH, three times with Et₂O, and dried under reduced pressure. Yield: 704 mg (7.50 × 10⁻⁴ mol, 75%). IR (KBr): $\tilde{\nu}/\text{cm}^{-1}$ = 3642 w, 3083 w, 2976 w, 2856 m, 1603 s, 1576 m, 1462 s, 1429 m, 1093 vs, 1009 m, 956 m, 847 m, 780 s, 723 w, 623 s, 490 m. ESI-MS (+) (CH₂Cl₂): *m/z* = 361.2 [(susan^{6-Me}){Fe(μ-O)Fe}]²⁺. Anal. Found: C 44.90, H 5.76, N 11.51. Calcd. for [(susan^{6-Me}){Fe(μ-OH)₂Fe}](ClO₄)₂·H₂O C₃₆H₅₄N₈Cl₂Fe₂O₁₁: C 45.16, H 5.68, N 11.70.

Synthesis of [(susan^{6-Me}){Fe^{III}(μ-O)(μ-O₂)Fe^{III}}](ClO₄)₂·2H₂O. A solution of [(susan^{6-Me}){Fe^{II}(μ-OH)₂Fe^{II}}](ClO₄)₂ (63 mg, 6.7 × 10⁻⁵ mol) in CH₂Cl₂ (2 mL) was added to a solution of 25% aqueous ammonia (20 μL, 2.6 × 10⁻⁴ mol, 3.9 equiv) in MeOH (6 mL) at -15 °C. Pouring an O₂ stream of approximate 0.1 L min⁻¹ through this yellow solution for 1.5 h at -15 °C results in immediately color change to dark green followed by precipitation of a black microcrystalline solid, which was filtered off, washed three times with cold water, a small amount of cold MeOH, three times with Et₂O, and dried under reduced pressure. Yield: 52 mg (5.3 × 10⁻⁵ mol, 78%). Anal. Found: C 43.34, H 5.20, N 11.02. Calcd. for [(susan^{6-Me}){Fe^{III}(μ-O)(μ-O₂)Fe^{III}}](ClO₄)₂·2H₂O C₃₆H₅₄N₈Cl₂Fe₂O₁₃: C 43.30, H 5.55, N 11.22. For single-crystal X-ray diffraction and magnetic measurements, the sample was recrystallized by slow evaporation of a filtered (0.2 μm pores size PTFE filter) solution of [(susan^{6-Me}){Fe^{III}(μ-O)(μ-O₂)Fe^{III}}](ClO₄)₂·2H₂O (200 mg, 2.02 × 10⁻⁴ mol) in MeCN (20 mL) at -30 °C. The resulting black crystals of [(susan^{6-Me}){Fe^{III}(μ-O)(μ-O₂)Fe^{III}}](ClO₄)₂·0.85 MeCN·0.7 H₂O were filtered off, washed three times with cold water, three times with cold MeOH, three times with Et₂O, and dried under reduced pressure. Yield: 52 mg (5.2 × 10⁻⁵ mol, 26%). IR (KBr): $\tilde{\nu}/\text{cm}^{-1}$ = 3079 w, 2999 w, 2918 w, 2881 w, 2811 w, 1605s, 1573 w, 1466 s, 1454 s, 1090 vs, 1002 m, 955 m, 933 w, 842 m, 832 w, 788 s, 686 m, 624 s, 500 w, 447 w. ESI-MS (+) (CH₂Cl₂/MeCN): *m/z* = 377.1 [(susan^{6-Me}){Fe(μ-O)(μ-O₂)Fe}]²⁺. Anal. Found: C 44.66, H 5.21, N 12.27. Calcd. for [(susan^{6-Me}){Fe(μ-O)(μ-O₂)Fe}](ClO₄)₂·0.8MeCN·H₂O C_{37.0}H_{54.4}N_{8.8}Cl₂Fe₂O₁₂: C 44.97, H 5.46, N 12.27.

Data availability

The crystallographic data generated in this study have been deposited at the Cambridge Crystallographic Data Centre under accession codes 2072804–2072806 (www.ccdc.cam.ac.uk/data_request/cif). Experimental details on synthesis and crystal structure determination, details on DFT calculations, analysis of Mössbauer spectra, ESI-MS, thermal ellipsoid plots, Mössbauer spectra, UV-Vis spectra, rR spectra, X-ray crystallographic data (cif) generated in this study are provided in the Supplementary Information. Source data are available from the corresponding author upon request.

Received: 23 April 2021; Accepted: 17 February 2022;

Published online: 16 March 2022

References

- Jasniewski, A. J. & Que, L. Dioxygen activation by nonheme diiron enzymes: diverse dioxygen adducts, high-valent intermediates, and related model complexes. *Chem. Rev.* **118**, 2554–2592 (2018).
- Solomon, E. I. & Park, K. Structure/function correlations over binuclear non-heme iron active sites. *J. Biol. Inorg. Chem.* **21**, 575–588 (2016).
- Tinberg, C. E. & Lippard, S. J. Dioxygen activation in soluble methane monooxygenase. *Acc. Chem. Res.* **44**, 280–288 (2011).
- Merkx, M. et al. Dioxygen activation and methane hydroxylation by soluble methane monooxygenase: a tale of two irons and three proteins. *Angew. Chem. Int. Ed.* **40**, 2782–2807 (2001).
- Banerjee, R., Jones, J. C. & Lipscomb, J. D. Soluble methane monooxygenase. *Annu. Rev. Biochem.* **88**, 409–431 (2019).
- Shu, L. et al. An Fe²⁺O₂ diamond core structure for the key intermediate Q of methane monooxygenase. *Science* **275**, 515–518 (1997).
- Banerjee, R., Proshlyakov, Y., Lipscomb, J. D. & Proshlyakov, D. A. Structure of the key species in the enzymatic oxidation of methane to methanol. *Nature* **518**, 431–434 (2015).
- Cutsail, G. E. et al. High-resolution extended X-ray absorption fine structure analysis provides evidence for a longer Fe–Fe distance in the Q intermediate of methane monooxygenase. *J. Am. Chem. Soc.* **140**, 16807–16820 (2018).
- Lee, S. K. & Lipscomb, J. D. Oxygen activation catalyzed by methane monooxygenase hydroxylase component: proton delivery during the O–O bond cleavage steps. *Biochemistry* **38**, 4423–4432 (1999).
- Tinberg, C. E. & Lippard, S. J. Revisiting the mechanism of dioxygen activation in soluble methane monooxygenase from *M. capsulatus* (Bath): evidence for a multi-step, proton-dependent reaction pathway. *Biochemistry* **48**, 12145–12158 (2009).
- Brunold, T. C., Tamura, N., Kitajima, N., Morooka, Y. & Solomon, E. I. Spectroscopic study of [Fe₂(O₂)(OBz)(HB(pz)⁺)₃]₂: nature of the μ -1,2 peroxide-Fe(III) bond and its possible relevance to O₂ activation by nonheme iron enzymes. *J. Am. Chem. Soc.* **120**, 5674–5690 (1998).
- Korboukh, V. K., Li, N., Barr, E. W., Bollinger, J. M. & Krebs, C. A long-lived, substrate-hydroxylating peroxodiiron(III/III) intermediate in the amine oxygenase, AurF, from *Streptomyces thioluteus*. *J. Am. Chem. Soc.* **131**, 13608–13609 (2009).
- Li, N., Korboukh, V. K., Krebs, C. & Bollinger, J. M. Four-electron oxidation of p-hydroxylaminobenzoate to p-nitrobenzoate by a peroxodiferric complex in AurF from *Streptomyces thioluteus*. *Proc. Natl Acad. Sci. USA* **107**, 15722–15727 (2010).
- Wang, C. & Chen, H. Convergent theoretical prediction of reactive oxidant structures in diiron arylamine oxygenases AurF and CmlI: peroxo or hydroperoxo? *J. Am. Chem. Soc.* **139**, 13038–13046 (2017).
- Park, K. et al. Peroxide activation for electrophilic reactivity by the binuclear non-heme iron enzyme AurF. *J. Am. Chem. Soc.* **139**, 7062–7070 (2017).
- Bim, D. et al. Proton-electron transfer to the active site is essential for the reaction mechanism of soluble Δ 9-desaturase. *J. Am. Chem. Soc.* **142**, 10412–10423 (2020).
- Acheson, J. F., Bailey, L. J., Brunold, T. C. & Fox, B. G. In-crystal reaction cycle of a toluene-bound diiron hydroxylase. *Nature* **544**, 191–195 (2017).
- McBride, M. J. et al. A peroxodiiron(III/III) intermediate mediating both N-hydroxylation steps in biosynthesis of the N-nitrosourea pharmacophore of streptozotocin by the multi-domain metalloenzyme SznF. *J. Am. Chem. Soc.* **142**, 11818–11828 (2020).
- Jensen, K. P., Bell, C. B., Clay, M. D. & Solomon, E. I. Peroxo-type intermediates in class I ribonucleotide reductase and related binuclear non-heme iron enzymes. *J. Am. Chem. Soc.* **131**, 12155–12171 (2009).
- Srnec, M. et al. Structural and spectroscopic properties of the peroxodiferric intermediate of Ricinus communis soluble Δ 9 desaturase. *Inorg. Chem.* **51**, 2806–2820 (2012).
- Jasniewski, A. J., Komor, A. J., Lipscomb, J. D. & Que, L. Unprecedented (μ -1,1-Peroxo)diferric structure for the ambiphilic orange peroxo intermediate of the nonheme n-oxygenase CmlI. *J. Am. Chem. Soc.* **139**, 10472–10485 (2017).
- Zhang, X. et al. Structural and spectroscopic characterization of (μ -hydroxo or μ -oxo)(μ -peroxo)diiron(III) complexes: models for peroxo intermediates of non-heme diiron proteins. *J. Am. Chem. Soc.* **127**, 826–827 (2005).
- Ookubo, T. et al. cis- μ -1,2-Peroxo diiron complex: structure and reversible oxygenation. *J. Am. Chem. Soc.* **118**, 701–702 (1996).
- Kim, K. & Lippard, S. J. Structure and Mössbauer spectrum of a (μ -1,2-Peroxo)bis(μ -carboxylato)diiron(III) model for the peroxo intermediate in the methane monooxygenase hydroxylase reaction cycle. *J. Am. Chem. Soc.* **118**, 4914–4915 (1996).
- Dong, Y., Yan, S., Young, V. G. & Que, L. Crystal structure analysis of a synthetic non-heme diiron-O₂ adduct: insight into the mechanism of oxygen activation. *Angew. Chem. Int. Ed. Engl.* **35**, 618–620 (1996).
- Sekino, M. et al. New mechanistic insights into intramolecular aromatic ligand hydroxylation and benzyl alcohol oxidation initiated by the well-defined (μ -peroxo)diiron(III) complex. *Chem. Commun.* **53**, 8838–8841 (2017).
- Kodera, M. et al. Synthesis, characterization, and activation of thermally stable μ -1,2-peroxodiiron(III) complex. *Inorg. Chem.* **40**, 4821–4822 (2001).
- Kodera, M., Itoh, M., Kano, K., Funabiki, T. & Reglier, M. A diiron center stabilized by a bis-TPA ligand as a model of soluble methane monooxygenase: predominant alkene epoxidation with H₂O₂. *Angew. Chem. Int. Ed.* **44**, 7104–7106 (2005).
- Fiedler, A. T. et al. Spectroscopic and computational studies of (μ -oxo)(μ -1,2-peroxo)diiron(III) complexes of relevance to nonheme diiron oxygenase intermediates. *J. Phys. Chem. A* **112**, 13037–13044 (2008).
- Xue, G., Fiedler, A. T., Martinho, M., Munck, E. & Que, L. Jr. Insights into the P-to-Q conversion in the catalytic cycle of methane monooxygenase from a synthetic model system. *Proc. Natl Acad. Sci. USA* **105**, 20615–20620 (2008).
- Do, L. H., Xue, G., Que, L. Jr. & Lippard, S. J. Evaluating the identity and diiron core transformations of a (μ -oxo)diiron(III) complex supported by electron-rich tris(pyridyl-2-methyl)amine ligands. *Inorg. Chem.* **51**, 2393–2402 (2012).
- Kodera, M. et al. Reversible O–O bond scission of peroxodiiron(III) to high-spin oxodiiron(IV) in dioxygen activation of a diiron center with a bis-tpa dinucleating ligand as a soluble methane monooxygenase model. *J. Am. Chem. Soc.* **134**, 13236–13239 (2012).
- Kryatov, S. V. et al. Dioxygen binding to complexes with Fe^{II}(μ -OH)₂ cores: steric control of activation barriers and O₂-adduct formation. *Inorg. Chem.* **44**, 85–99 (2005).
- MacMurdo, V. L., Zheng, H. & Que, L. Jr. Model for the cofactor formation reaction of *E. Coli* ribonucleotide reductase. from a Diiron(II) precursor to an Fe^{III}Fe^{IV} species via a peroxo intermediate. *Inorg. Chem.* **39**, 2254–2255 (2000).
- Török, P. et al. A nonheme peroxo-diiron(III) complex exhibiting both nucleophilic and electrophilic oxidation of organic substrates. *Dalton Trans.* **50**, 7181–7185 (2021).
- Cranswick, M. A. et al. Protonation of a peroxodiiron(III) complex and conversion to a diiron(III/IV) intermediate: implications for proton-assisted O–O bond cleavage in nonheme diiron enzymes. *Inorg. Chem.* **51**, 10417–10426 (2012).
- Strautmänn, J. B. H. et al. Design and synthesis of a dinucleating ligand system with varying terminal donor functions that provides no bridging donor and its application to the synthesis of a series of Fe^{III}- μ -O-Fe^{III} complexes. *Dalton Trans.* **45**, 3340–3361 (2016).
- Glaser, T. A dinucleating ligand system with varying terminal donor functions but without bridging donor functions: Design, synthesis, and applications for diiron complexes. *Coord. Chem. Rev.* **380**, 353–377 (2019).
- Walleck, S. & Glaser, T. A dinucleating ligand system with varying terminal donors to mimic diiron active sites. *Isr. J. Chem.* **60**, 1019–1031 (2020).
- Zimmermann, T. P., Dammers, S., Stammler, A., Bögge, H. & Glaser, T. Reactivity differences for the oxidation of Fe^IFe^{II} to Fe^{III}(μ -O)Fe^{III} complexes caused by pyridyl versus 6-methyl-pyridyl ligands. *Eur. J. Inorg. Chem.* **48**, 5229–5237 (2018).
- Broadwater, J. A., Achim, C., Münck, E. & Fox, B. G. Mössbauer studies of the formation and reactivity of a quasi-stable peroxo intermediate of stearoyl-acyl carrier protein Delta 9-desaturase. *Biochemistry* **38**, 12197–12204 (1999).
- Gorun, S. M. & Lippard, S. J. Magnetostructural correlations in magnetically coupled (μ -oxo)diiron(III) complexes. *Inorg. Chem.* **30**, 1625–1630 (1991).
- Weihe, H. & Güdel, H. U. Angular and distance dependence of the magnetic properties of oxo-bridged iron(III) dimers. *J. Am. Chem. Soc.* **119**, 6539–6543 (1997).
- Glaser, T. et al. S K-edge absorption studies of tetranuclear iron-sulfur clusters; μ -sulfide bonding and its contribution to electron delocalization. *J. Am. Chem. Soc.* **123**, 442–454 (2001).
- Zimmermann, T. P. et al. Reversible Carboxylate Shift in a μ Oxo Diferric Complex in Solution by Acid-/Base-Addition. *Inorg. Chem.* **57**, 5400–5405 (2018).
- Ballhausen, C. J. *Introduction to Ligand Field Theory* (McGraw-Hill, New York, 1962).
- Bencini, A. & Gatteschi, D. *Electron Paramagnetic Resonance of Exchanged Coupled Systems* (Springer, Berlin, 1990).
- Robin, M. B. & Day, P. Mixed-valence chemistry: a survey and classification. *Adv. Inorg. Chem. Radiochem.* **10**, 247–422 (1967).
- Job, P. Studies on the formation of complex minerals in solution and on their stability. *Ann. Chim. France*, **9**, 113–203 (1928).
- Vosburgh, W. C. & Cooper, G. R. Complex Ions. I. The Identification of complex ions in solution by spectrochemical measurements. *J. Am. Chem. Soc.* **63**, 437–442 (1941).
- Wertz, D. L. & Valentine, J. S. Nucleophilicity of iron-peroxo porphyrin complexes. *Struc. Bond.* **97**, 37–60 (2000).
- Annaraj, J., Suh, Y., Seo, M. S., Kim, S. O. & Nam, W. Mononuclear nonheme ferric-peroxo complex in aldehyde deformylation. *Chem. Commun.*, **2005**, 4529–4531 (2005).
- Ohmori, H., Nakai, S. & Masui, M. Anodic oxidation of organophosphorus compounds. Part 1. Anodic alkylation of triphenylphosphine. *J. Chem. Soc., Perkin Trans. 1*, 1333 (1978).

54. Tshepelevitsh, S. et al. On the basicity of organic bases in different media. *Eur. J. Org. Chem.* **2019**, 6735–6748 (2019).
55. Chandra, A. et al. Ligand-constraint-induced peroxide activation for electrophilic reactivity. *Angew. Chem. Int. Ed.* **60**, 14954–14959 (2021).
56. Bordwell, F. G., Cheng, J. P. & Harrelson, J. A. Homolytic bond dissociation energies in solution from equilibrium acidity and electrochemical data. *J. Am. Chem. Soc.* **110**, 1229–1231 (1988).
57. Warren, J. J., Tronic, T. A. & Mayer, J. M. Thermochemistry of proton-coupled electron transfer reagents and its implications. *Chem. Rev.* **110**, 6961–7001 (2010).
58. Wise, C. F., Agarwal, R. G. & Mayer, J. M. Determining proton-coupled standard potentials and X-H bond dissociation free energies in nonaqueous solvents using open-circuit potential measurements. *J. Am. Chem. Soc.* **142**, 10681–10691 (2020).
59. Luo, Y.-R. *Comprehensive Handbook of Chemical Bond Energies* (CRC Press, 2007).
60. Gerken, J. B., Pang, Y. Q., Lauber, M. B. & Stahl, S. S. Structural effects on the pH-dependent redox properties of organic nitroxyls: pourbaix diagrams for TEMPO, ABNO, and three TEMPO analogs. *J. Org. Chem.* **83**, 7323–7330 (2018).
61. Zimmermann, T. P. et al. Two unsupported terminal hydroxo ligands in a μ -Oxo-bridged ferric dimer: protonation and kinetic lability studies. *Inorg. Chem.* **57**, 10457–10468 (2018).
62. Zimmermann, T. P. et al. Catalytic H₂O₂ activation by a diiron complex for methanol oxidation. *Inorg. Chem.* **59**, 15563–15569 (2020).
63. Goodson, P. A., Oki, A. R., Glerup, J. & Hodgson, D. J. Design, synthesis, and characterization of bis(μ -oxo)dimanganese(III,III) complexes. Steric and electronic control of redox potentials. *J. Am. Chem. Soc.* **112**, 6248–6254 (1990).
64. Nagao, H., Komeda, N., Mukaida, M., Suzuki, M. & Tanaka, K. Structural and electrochemical comparison of copper(II) complexes with tripodal ligands. *Inorg. Chem.* **35**, 6809–6815 (1996).
65. Benhamou, L., Lachkar, M., Mandon, D. & Welter, R. The preparation and full characterization of dichloroiron complexes of mono-, bis- and tris-alpha-methyl substituted tris(2-pyridylmethyl)amine (TPA) ligands. Structural bases of stability of the complexes in solution. *Dalton Trans.*, 6996–7003 (2008).
66. Suzuki, M. Ligand effects on dioxygen activation by copper and nickel complexes. *Reactivity Intermed. Acc. Chem. Res.* **40**, 609–617 (2007).
67. Prat, I. et al. Assessing the impact of electronic and steric tuning of the ligand in the spin state and catalytic oxidation ability of the Fe(II)(Pytacn) family of complexes. *Inorg. Chem.* **52**, 9229–9244 (2013).
68. Zang, Y. et al. Models for nonheme iron intermediates. structural basis for tuning the spin states of Fe(TPA) complexes. *J. Am. Chem. Soc.* **119**, 4197–4205 (1997).
69. Zheng, H., Yoo, S. J., Münch, E. & Que, L. The flexible Fe₂(μ -O)₂ diamond core: a terminal iron(IV)–oxo species generated from the oxidation of a Bis(μ -oxo)diiron(III) complex. *J. Am. Chem. Soc.* **122**, 3789–3790 (2000).
70. Skulan, A. J. et al. Nature of the peroxo intermediate of the W48F/D84E ribonucleotide reductase variant: Implications for O-2 activation by binuclear non-heme iron enzymes. *J. Am. Chem. Soc.* **126**, 8842–8855 (2004).

Acknowledgements

T.G. acknowledges Bielefeld University of financial support.

Author contributions

S.W. conducted all syntheses, oxidation experiments, protonation experiments, reactivity studies, characterizations not otherwise mentioned here, and the DFT calculations. T.Z. conducted the initial syntheses of the peroxo-diferric complex. S.W., H.H., C.P. and S.K. recorded and analyzed the resonance Raman data. T.H. and P.H. assisted with the analysis of the resonance Raman data. A.S. and H.B. collected, solved, and refined all the crystallographic data. E.B. recorded and interpreted the EPR and magnetic Mössbauer data. T.G. designed experiments, assisted with data analysis, and wrote the manuscript with input from all the authors.

Funding

Open Access funding enabled and organized by Projekt DEAL.

Competing interests

The authors declare no competing interests.

Additional information

Supplementary information The online version contains supplementary material available at <https://doi.org/10.1038/s41467-022-28894-5>.

Correspondence and requests for materials should be addressed to Thorsten Glaser.

Peer review information *Nature Communications* thanks the anonymous reviewer(s) for their contribution to the peer review of this work. Peer reviewer reports are available.

Reprints and permission information is available at <http://www.nature.com/reprints>

Publisher's note Springer Nature remains neutral with regard to jurisdictional claims in published maps and institutional affiliations.



Open Access This article is licensed under a Creative Commons Attribution 4.0 International License, which permits use, sharing, adaptation, distribution and reproduction in any medium or format, as long as you give appropriate credit to the original author(s) and the source, provide a link to the Creative Commons license, and indicate if changes were made. The images or other third party material in this article are included in the article's Creative Commons license, unless indicated otherwise in a credit line to the material. If material is not included in the article's Creative Commons license and your intended use is not permitted by statutory regulation or exceeds the permitted use, you will need to obtain permission directly from the copyright holder. To view a copy of this license, visit <http://creativecommons.org/licenses/by/4.0/>.

© The Author(s) 2022